FY2015 Enhanced Surveillance Annual Report (ESAR) Instructions and Template

Overview:

The Enhanced Surveillance Sub-program has an annual NNSA requirement to submit a comprehensive report on all our fiscal year activities right after the start of the next calendar year. As most of you know, we collate all of our PI task submissions into a single volume that we send to NNSA, our customers, and use for other programmatic purposes. The functional objective of this report is to formally document the purpose, status, and accomplishments and impacts of all our work.

For your specific submission, please follow the instructions described below and use the template provided. These are essentially the same as was used last year.

We recognize this report may also include information on specific age-related findings that you will provide again in a few months as input to the Stockpile Annual Assessment process (e.g., in the submittal of your Component Assessment Report). However, the related content of your ES AR input should provide an excellent foundation that can simply be updated as needed for your Annual Assessment input.

Instructions:

- **Report Content:**
  Using the template attached below, include documentation for each section. As applicable, consider content of previous inputs to quarterly status reporting. If the information requested is already contained in another published and referenced report (e.g., SAND), that information can simply be summarized in the task report with a reference included to that alternate report. Duplicating properly documented information is unnecessary.

- **Report Length:**
  The length of this report should be consistent with the scope of your task(s) and cover all significant activity performed in FY15. If some of the information has already been documented in a referenced report as noted in the previous paragraph, a shorter summary-type submission is acceptable. The opposite option is to include an in-depth report which has historically been typically followed.

- **Formatting**
    - Use Calibri, 11 point font for text, left paragraph justification, and submit your report in Word (docx or doc) format.
        - **** Note to Mac users:** Ensure your document and figures translate properly to a PC, as final processing will be done on a PC.
    - Figures and captions can be included within the text or placed at the end of the report.
        - ****Note:** Be mindful of embedded objects such those associated with pasting in from Minitab and Excel files. Typically, figures are best incorporated by pasting them in as pictures. Embedded objects usually make your file excessively large and difficult to merge with others in the final report.
    - The highlighted portions of the document template are the only areas that you can use or change. This restriction is to ensure your document is automatically and correctly formatted. You can add bullets and numbered list while the font format should remain the same.

- **Special Considerations**
  - Any QMU analyses that are included in your ES AR submission must have first completed a formal review and approval process (per QMU handbook).

- **Formal R&A Review**

  Prior to final transfer of your report to the ES program manager, your task report (for both unclassified and classified) must be submitted into the SNL R&A process (formal review): https://eims.sandia.gov/RAA/home.jsp. Complying with this requirement will document that a DC, the PI's manager, and a classification analyst have properly reviewed the report prior to submission and that it is properly marked.

- **Submission**

  Please submit your task report by emailing it to: 1) Regan Stinnett, ES program manager, and 2) Lynne Felix, ISE Planning Operations Lead .

  Include the following information in the email:
  - SAND number from the formal R&A process (e.g., SAND2015-xxxx),
  - name of the DC,
  - name of the classification analyst,
  - classification level

  - <u>Unclassified reports</u>: send to **Regan Stinnett (rwstinn@sandia.gov)** and **Lynne Felix (lfelix@sandia.gov)**
  - <u>Classified reports</u>: send via classified email to **Regan Stinnett (rwstinns@sandia.gov)**, and **Lynne Felix (lfelixs@sandia.gov)**

<div align="center">

Due date is Thursday, September 24, 2015

</div>

Hydrogen Assisted Fracture of Stainless Steels
96099/80.401.82.01

Brian Somerday, Josh Sugar, Mark Homer, Suzy Vitale, and Junko Matsuda
Sandia National Laboratories
Livermore, CA 94551

Abstract

Two notable accomplishments are described in this FY15 report: 1) we have developed a hypothesis for the effects of environment on deformation mechanisms in 21-6-9 austenitic stainless steels, and 2) new capabilities for more rigorously quantifying the characteristics of deformation microstructures were established at SNL CA. Based on conventional methods for characterizing deformation microstructures in 21-6-9 stainless steel, we propose that the deformation is accompanied by the formation of dislocations, which eventually separate into stacking faults. The stacking faults then widen as additional dislocations add one atomic plane at a time to the fault, eventually forming a deformation twin. The presence of hydrogen reduces the ability for the dislocations to cross slip and glide, resulting in thinner twins that may contribute to microcrack formation. In the future, we will continue to develop our new capabilities and methodologies to test our hypothesis and refine it to account for effects of grain orientation on twin characteristics such as thickness. These methodologies employ a new focused ion beam (FIB) device to apply state-of-the-art techniques, such as such as electron backscatter diffraction (EBSD) and preparation of electron-transparent samples from site-specific locations. Ultimately, understanding the deformation mechanism is a critical step in the development of predictive hydrogen-assisted cracking models that can be used to evaluate the long-term aging performance of stainless steels in hydrogen isotope environments relevant to gas transfer systems (GTS).

Introduction

The aging-related degradation of stainless steels in hydrogen environments (i.e., hydrogen embrittlement) is a well-known problem having a negative impact on the long-term performance of containment materials in hydrogen storage applications. This has direct implications for the safety and reliability of hydrogen isotope containment reservoirs in gas transfer systems (GTS). Previous results have suggested that hydrogen-assisted cracking in stainless steels is directly linked to deformation [1, 2] because microcracks form in regions of strain localization. Therefore, understanding the deformation mechanism in these materials before the onset of fracture, and the effect of hydrogen on that mechanism, enables formulation of a physical description of hydrogen-assisted cracking in stainless steels, which is a necessary first step in developing a predictive model. Our goal here is to understand the deformation mechanism in a simpler variant of the stainless steels in GTS reservoirs, annealed 21-6-9 alloy, so that we can use this information to develop physical descriptions of hydrogen-assisted cracking in more complex stainless steels. By focusing on 21-6-9 initially, we increase our chances for success because deformation-induced martensite does not form and complicate the microstructure as it does in 304 or 316 stainless steels, for example. Eventually, we hope to extend our understanding of deformation mechanisms to these other alloys.

Approach

Our general approach involves looking at the internal microstructure of sections of tensile bars of 21-6-9. A tensile specimen matrix was generated in which a total of 12 tests were designed at two hydrogen concentrations, at two temperatures, and at three strains. This is summarized in the test specimen matrix table below.

Table 1: Deformation Study Test Specimen Matrix

Sample	H Concentration (wppm)	Strain (%)	Temperature (°C)
94L-27	0	35	23
94L-28	0	20	23
94L-29	0	5	23
94L-9	220	35	23
94L-10	220	20	23
94L-11	220	5	23
94L-33	0	35	-50
94L-34	0	20	-50
94L-35	0	5	-50
94L-21	220	35	-50
94L-22	220	20	-50
94L-23	220	5	-50

By comparing the deformation microstructures at different strain levels and under different environmental conditions, we expect to observe trends so that we can hypothesize and test possible mechanisms. To accomplish this, we remove thin discs from the gauge section of tensile bars and electropolish them to electron transparency so that we can view the microstructures in the TEM. In the TEM, we are able to compare microstructural features such as stacking faults, twins, and dislocations under different environmental and loading conditions. In the past, we have chosen a statistical approach and looked at microstructures that we could find in thin areas of the sample. We tilt the sample to a preferential crystallographic orientation to view defects, and then image the defects in these orientations.

After a careful evaluation of our approach, we realized that it required some improvement. It is necessary to track the orientation of the tensile axis relative to the crystallographic orientation of the grain being viewed in the TEM. It is known that the crystallographic orientation of a grain relative to the tensile axis affects the deformation response. As an example, some crystallographic orientations in steel are softer than others [3], therefore it would be expected that the deformation microstructure could vary considerably as one investigates different grain orientations relative to the tensile axis. In our efforts to improve our approach, we have developed 3 new methodologies for investigating these deformation structures. The goal was to be more systematic about the trends we looked for in these microstructures and to ensure that similar grain orientations are compared at the different levels of strain. These will be described below.

New Methodologies for Orientation Dependent Analysis of Deformation Structures in 21-6-9
Method 1: The first method to tracking grain orientation relative to the tensile axis starts with the assumption that all thin-disc samples are cut perpendicular to the tensile axis. This is shown schematically in Figure 1.
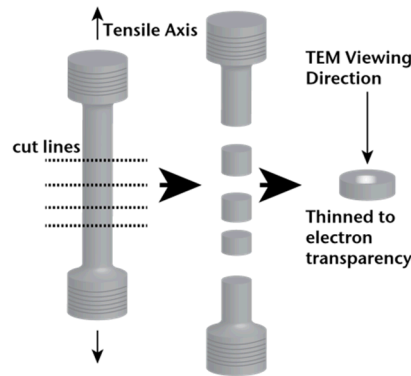
Figure 1: Schematic showing steps for TEM sample preparation. With this method, it is assumed that the tensile axis is perpendicular to the TEM viewing direction.

It is unlikely that the cuts are perfectly perpendicular to the tensile axis, so there is some error associated with assuming perpendicular cuts. However, when performing the TEM analysis, it is possible to document the sample tilt needed to obtain a specific crystallographic orientation parallel to the viewing direction within one grain. In this way, it is possible to look for grains with similar orientations relative to the tensile axis in samples with different strains. This method is limited, however, by the fact that it relies on the random grains that can be found and tilted to a preferential orientation in the TEM. Because this requires investigating each grain individually, it can be time consuming and inefficient. This method is summarized in Figure 2.
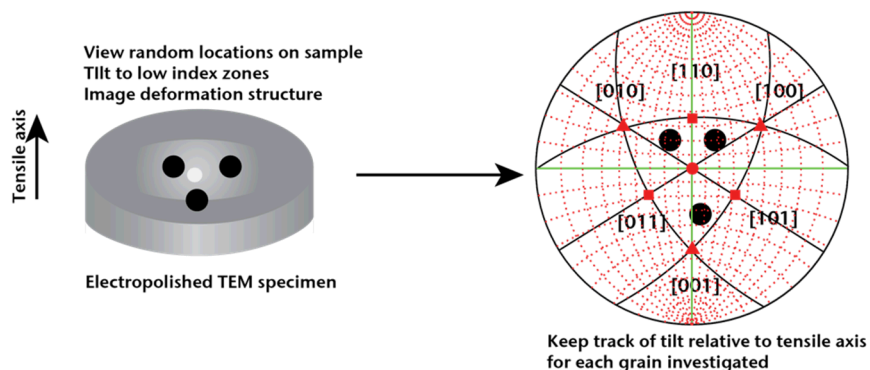

Figure 2: Schematic showing the general method for investigating different orientations of grains relative to the tensile axis using only the TEM. Regions are selected at random in the sample and tilted to low index zones. The tilt is recorded and later can be compared to the tensile axis to map the orientation of the grains.

Method 2: Recently, the NW community at SNL CA has made major investments in new material characterization capabilities. These new capabilities have opened the door to methods for obtaining systematic information in samples such as ours. Specifically, SNL CA has acquired a new dual beam FIB-SEM (focused ion beam-scanning electron microscope) with analytical EDS and EBSD detectors. EDS (energy dispersive spectroscopy) provides compositional information while EBSD (electron back-scattered diffraction) provides crystallographic orientation information. Increased access to EBSD capability is greatly enhancing our ability and efficiency with which we can track deformation structures in stainless steels. One way in which we can use this capability to our advantage is by mapping the orientation of grains in an electropolished TEM sample. This means that we use EBSD to map the

orientation of the grains in our TEM sample, then we focus our attention only on the grains that have crystallographic orientations relative to the tensile axis that we are interested in investigating. This means that time that would have to be spent tilting grains of unknown crystallographic orientation in the TEM is reduced, time is used more efficiently, and a more systematic approach to investigating the various orientations is enabled. This method is shown schematically in Figure 3.
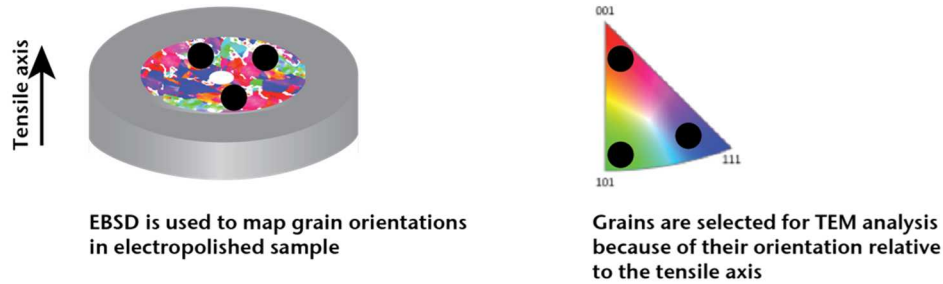

EBSD is used to map grain orientations in electropolished sample

Grains are selected for TEM analysis because of their orientation relative to the tensile axis

Figure 3: Schematic showing a more systematic approach to investigation of deformation structures in stainless steels that utilizes EBSD and TEM. EBSD is used to map the crystallographic orientations of grains in an electropolished and thin TEM specimen. Regions having an orientation of interest relative to the tensile axis are selected and investigated further in the TEM.

Method 3: The final methodology we develop here is enabled by combining both EBSD and the nanoscale material removal capabilities of the FIB-SEM. In this case, a section of the tensile bar is removed and characterized prior to making electropolished TEM specimens. EBSD is used to map the orientations of the grains in the section relative to the tensile axis. Then, certain grains are selected for their orientation, and the FIB-SEM is used to prepare electron transparent samples. This is shown schematically in Figure 4.

EBSD is used to map grain orientations in section of tensile bar

Specific crystallographic oreintations relative to the tensile axis are selected, thinned, and lifted out as thin TEM specimens using FIB
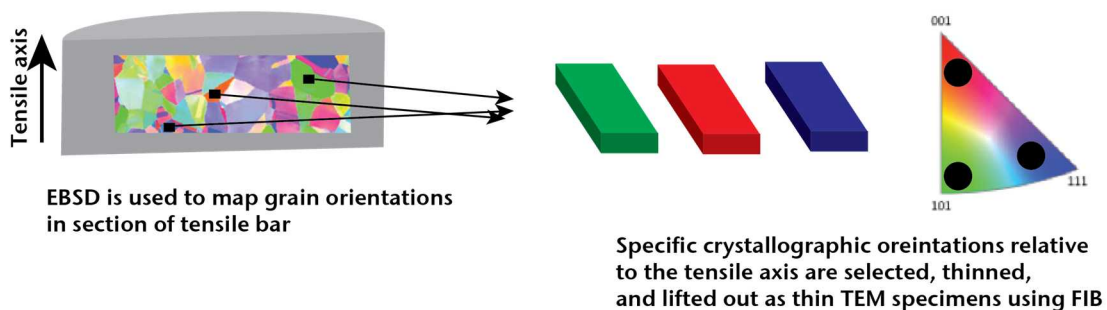
Figure 4: Schematic showing a systematic approach to investigate deformation structures in stainless steels that utilizes EBSD, FIB-SEM, and TEM. First, EBSD is performed on a section of the tensile bar to map the grain orientations in the specimen. Then, regions are selected because of their orientation relative to the tensile axis. These regions are then thinned into electron transparent samples using the FIB-SEM.

This final method is very powerful, but has the disadvantage that the FIB-SEM preparation process has the potential to introduce artifacts into the sample that change the deformation structure. While both electropolishing and FIB-SEM are well-accepted ways to prepare thin TEM samples, and both of them have the potential to introduce artifacts, we are more familiar with electropolishing artifacts than those

introduced by the FIB-SEM because of our historical experience. Therefore, we must do our due diligence when investigating these samples to ensure that we are not simply observing sample preparation artifacts.

Observed Mechanisms of Deformation in 21-6-9

While our previous work did not use the systematic methodologies we are developing here, we were able to observe some general trends in our previous work that enables us to make hypotheses about the deformation microstructure development in 21-6-9 stainless steel. In previous years, we used method 1 to investigate these samples. It is not possible to obtain a large quantity of statistics for different crystallographic orientations when we rely on finding random grains in the TEM that can be tilted to preferred viewing directions, but we did observe some trends in the samples that enabled hypothesizing about the deformation mechanisms active in these materials.

One general trend observed in the 21-6-9 stainless steel is that the formation of deformation twins seems to be associated with increased strain levels. This is most easily seen by investigation of the diffraction patterns , as shown in Figure 5 for the material with 0 ppm hydrogen strained at room temperature. Initially, at 5% strain, the diffraction pattern is a clean <110>-zone diffraction pattern (Figure 5 (d)). The corresponding BF image in Figure 5 (a) shows dislocations and linear features that have the appearance of planar defects along {111} planes. At the increased 20% strain level, the diffraction pattern (Figure 5 (e)) shows streaks (in red) parallel to a 111-diffraction vector ($\mathbf{g_{111}}$). In the BF image (Figure 5 (b)), there are so many defects visible in the image it is practically impossible to see through the sample. Again, there appear to be linear features in the image parallel to {111} planes and dislocations distributed throughout the image in a fairly high density. Finally, the diffraction pattern corresponding to 35% strain, shown in Figure 5 (f) shows the expected diffraction pattern for a <110> zone axis with twin reflections (one of which is circled in red). The BF image in Figure 5 (c) shows dark bands running left-to-right in the image that are consistent with the twin reflections in (f). This is confirmed by the dark-field image in (g) and the simulated diffraction pattern in (h).
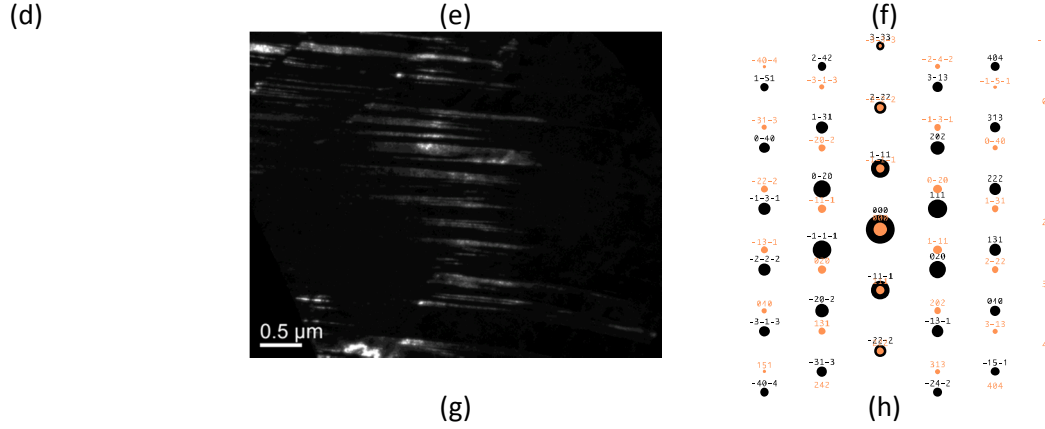

| (a) | (b) | (c) |

(d)　　　　　　　　(e)　　　　　　　　(f)

0.5 µm

(g)　　　　　　　　　　　　　　　　(h)
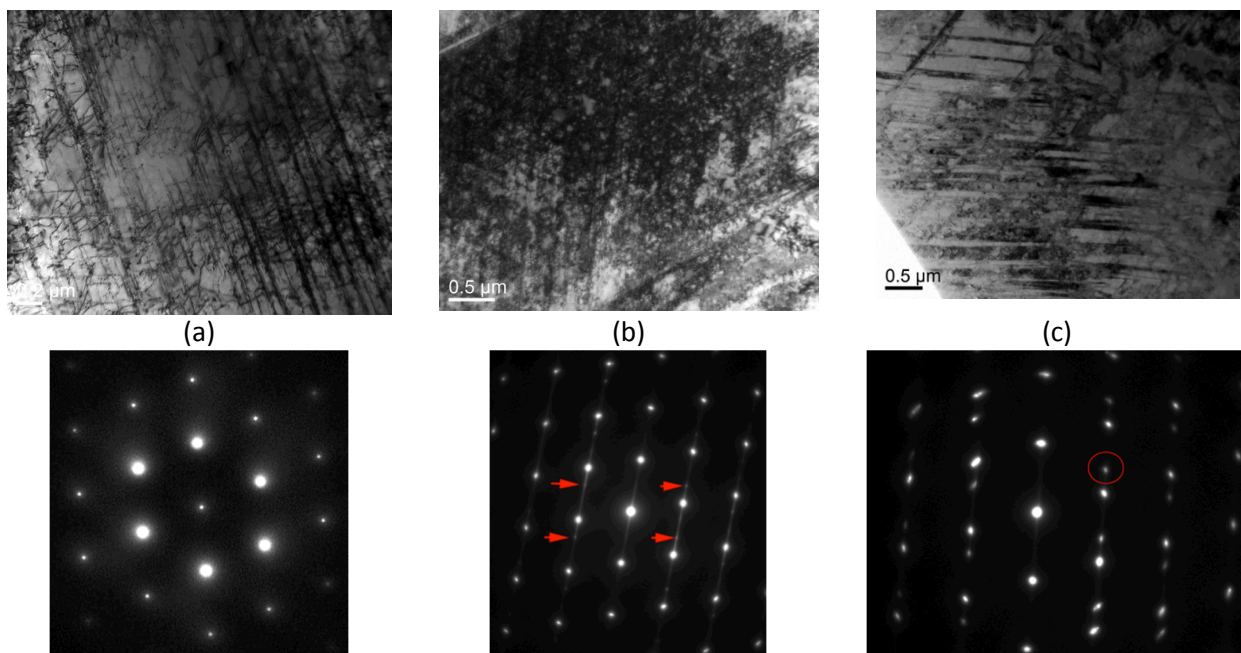
Figure 5: Bright-field (BF) TEM images (a) – (c) and corresponding diffraction patterns (d) – (f) for samples with 0 ppm hydrogen and strained to 5%, 20%, and 35%, respectively, at room temperature. All diffraction patterns are acquired in a <110>-type zone viewing direction. The dark-field image in (g) shows features that are bright corresponding to the circled reflection in (f). This confirms that the dark horizontal bands in (c) are twins. The simulated diffraction pattern in (h) shows the twin reflections in orange.

The observations made from Figure 5 can be summarized with the statement that high strains in this material cause the formation of deformation twins through an intermediate step of planar defects. Certainly, at high strains the diffraction pattern clearly shows twins. At intermediate strains (20%), however, the diffraction pattern has streaks in it, these streaks are likely the initial formation of twins that are only a small number of atomic layers thick. So, as strain is increased from 5% to 35%, we see linear features in the image representing defects that start being visible when they are 10 nm wide, but increase in width to approximately 100 nm. In addition, dislocations are visible at low strains, but at the highest strains, individual dislocation lines are less visible. This suggests a deformation mechanism in which dislocation motion, enabled by cross slip, can interact with twins and cause them to widen. This mechanism is summarized in Figure 6.
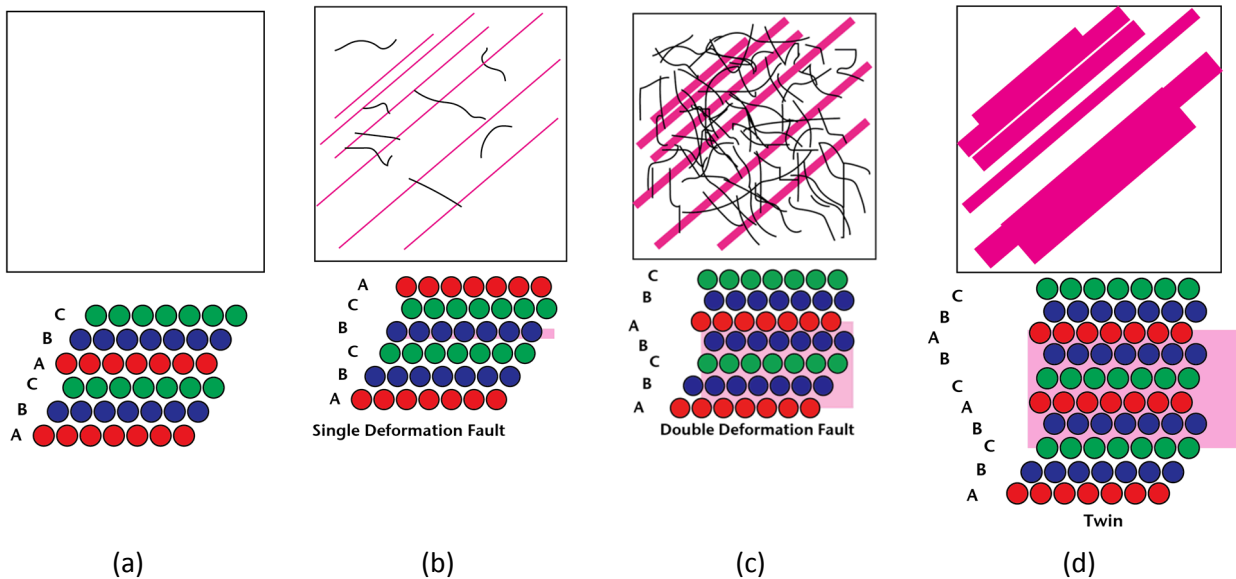

(a)　　　　　　　(b)　　　　　　　(c)　　　　　　　(d)

Figure 6: Schematic showing the hypothesized deformation mechanism for 21-6-9 with 0 ppm hydrogen.

First, (a) the perfect idealized fcc close-packed structure is shown and an image with no contrast. In (b), a single deformation stacking fault has formed, causing the straight magenta features in the image. Dislocations lines are also visible (black). In (c), the dislocation density has increased and the deformation faults have also doubled, presumably by the cross slip of dislocations to the fault interface widening it by one atomic plane. This also causes widening of the magenta features in the image, and potential streaking in the diffraction pattern. The deformation faults continue to grow by one atomic plane at a time, and form twins as in (d), which are now wide fault regions and cause twin reflections in the diffraction pattern.

We have observed evidence previously that suggests that twinned regions have interfacial steps that are a few atomic planes wide at the twin interface. This is shown in Figure 7. The arrow points to an interfacial step at a twinned region that is a few atomic planes wide. Each time an individual dislocation glides to the twin interface, the twin can widen by one atomic step. This is also supported by observations in the literature that show that dislocations can separate into two partials and form a stacking fault [4]. The mechanism in Figure 6 shows how multiple stacking faults can combine to eventually form a twinned region in the microstructure.
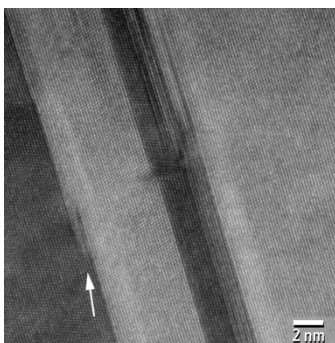

Figure 7: HRTEM image of a twin in 21-6-9 with 220 ppm hydrogen strained to 20% at room temperature. The twin is roughly 5 nm wide, and an interfacial step is seen, which is evidence that the twins widen by a dislocation glide mechanism.

The next important question is what effect does hydrogen have on this deformation mechanism? When samples with 220 ppm hydrogen are observed in the same way as samples with 0 ppm hydrogen, similar types of microstructural defects are observed. However, the twins in hydrogen-exposed samples do not appear to develop to the same width as they do in non-exposed samples. Examples of this are shown in Figure 8. The same development of long planar defects is visible as well as the development of streaks and twin reflections in the diffraction patterns. The main differences between the hydrogen-exposed and non-exposed samples are that the twins do not get as wide when hydrogen is present (30 nm wide with 220 ppm hydrogen versus 100 nm wide with 0 ppm hydrogen) and the dislocation density in the 35% strained, hydrogen-exposed sample is still significant such that the contrast in the image is almost completely dark (similar to 20%, non-exposed sample).
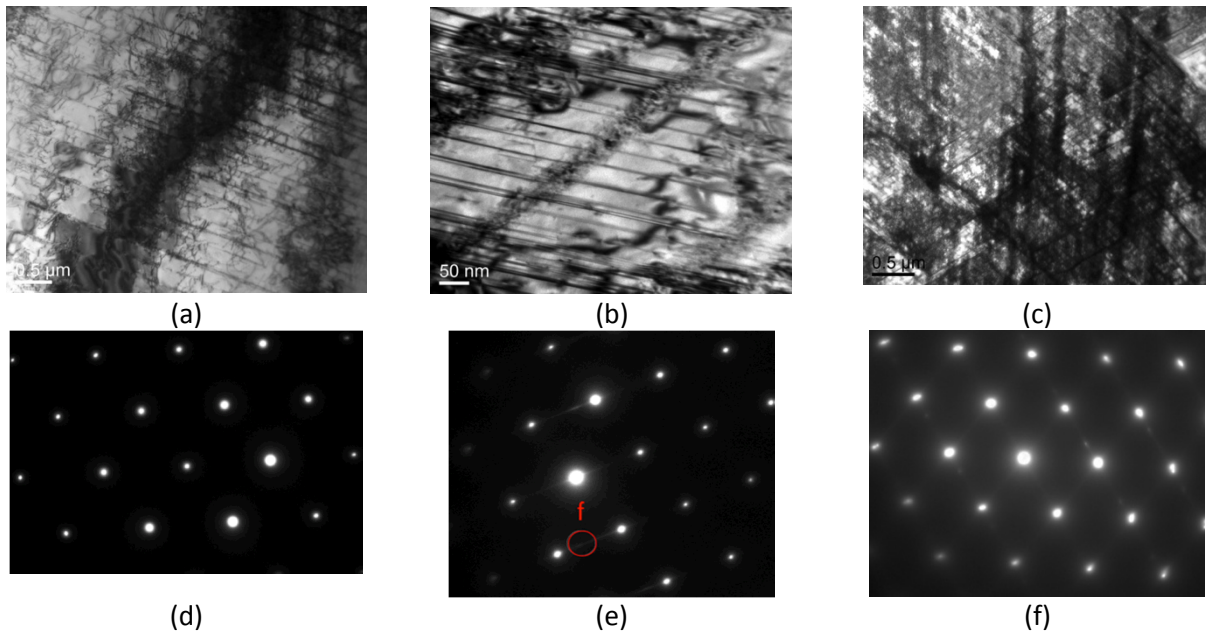
Figure 8: Bright-field (BF) TEM images (a) – (c) and corresponding diffraction patterns (d) – (f) for samples with 220 ppm hydrogen and strained to 5%, 20%, and 35% strain, respectively, at room temperature.

The development of deformation faults and twins requires the cross slip and glide of dislocations. The presence of hydrogen is believed to strongly reduce the ability for dislocations to cross slip in stainless steel, enabling the development of localized deformation [5]. This suggests that the widening of twins is inhibited by hydrogen, and there may be an association between thinner twins and microcrack formation [6, 7]. This type of an effect is schematically shown in Figure 9 and would result in the eventual embrittlement of the material.
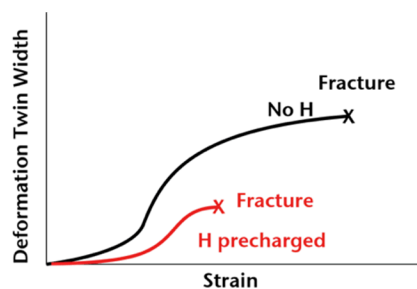
Figure 9: Schematic showing effect of hydrogen on the development of twins in 21-6-9. Because H inhibits the cross slip of dislocations, the twins can not get as wide in hydrogen-exposed samples. The thinner twins may be associated with formation of microcracks.

Effects of Low Temperature on Mechanisms of Deformation
Tensile tests at -50 °C also appear to show similar deformation mechanisms and microstructural development as samples strained at room temperature. It appears that temperature is another parameter that also affects the ability for dislocations to cross slip and affect the evolving microstructure. Some examples of this are shown in Figure 10.
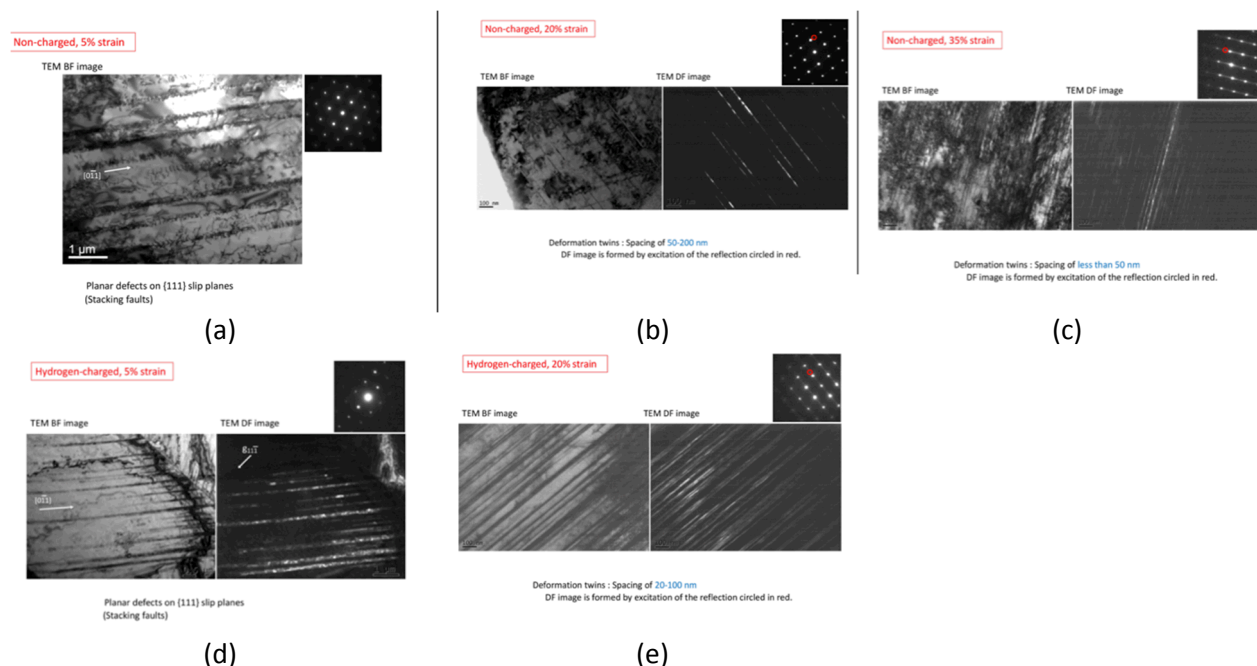
Figure 10: BF images and diffraction patterns from samples tested at -50°C of (a) 0 ppm hydrogen at 5% strain, (b) 0 ppm hydrogen at 20% strain, (c) 0 ppm hydrogen at 35% strain, (d) 220 ppm hydrogen at 5 % strain, and (e) 220 ppm hydrogen at 20% strain.

For samples tested at -50°C, the same types of trends are observed where deformation twins develop with increased strain levels. This is supported by the development of dark, straight bands in the BF images and streaks in the diffraction patterns of Figure 10. In addition, dark-field images formed from the streaks in the diffraction pattern cause the dark bands to turn bright, which suggests they are in fact features at the early stages of twin nucleation and development. However, none of the low-temperature data we have currently shows well-developed twins that are greater than or equal to 100 nm wide. At reduced temperature, regardless of hydrogen exposure, the twin width reaches a maximum of 10 – 30 nm. This suggests that temperature is another factor that can prevent cross slip of dislocations and effectively inhibit the widening of twins. It is not clear from our current data how hydrogen and temperature effects combine and alter deformation mechanisms. However, our data suggests that the deformation of an austenitic stainless steel system such as 21-6-9 is mostly governed by the development of deformation twins, and hydrogen and temperature may inhibit twin development by preventing cross slip, potentially contributing to microcrack formation.

All of the microstructural trends presented so far are qualitative and they do not take into account the crystallographic orientation of specific grains relative to the tensile axis. The problem is that different orientations of grains can behave softer than others. Therefore, one might expect that the width of the deformation twins will not only depend on strain but also grain orientation. This motivated the development of new methodologies and the use of new state-of-the art characterization capabilities to be more systematic about tracking twin width and crystallographic orientation. A major goal this year was to develop these methodologies, and the next section discusses progress on these new methodologies.

Progress on New Systematic Methodologies for Quantifying Deformation Microstructures in 21-6-9

Method 1: We have described three new methodologies for investigating deformation structures in austenitic stainless steels in a systematic manner. The first methodology simply involves tracking the tilt used during the imaging in the TEM and assuming that the perpendicular viewing direction is parallel to the tensile axis. Then, use of the stereographic projection enables visualizing the crystallographic orientation of the investigated grains relative to the tensile axis. In this particular case, we plot a point on the stereographic projection that corresponds to one image. The sample is tilted to a specific orientation inside the TEM to align a crystallographic orientation with the viewing direction. By recording the amount of x- and y- tilt for each image, we can then relate the orientation in the image relative to the sample perpendicular. If we assume the sample perpendicular is parallel to the tensile axis, then we know the orientation of the grain relative to the tensile axis. Stereographic projections that demonstrate this visualization technique are shown in Figure 11.

A comparison of the data in Figure 11 shows some of the limitations of using method 1 by itself. First, considering only the room temperature data, one can see that there was only one image in the hydrogen charged data that had a similar orientation to the tensile axis as the non-charged data. This points out the difficulty in comparing similar orientations when relying only on statistics and random sampling of data. The other limitation of the data is more easily demonstrated in the -50°C data, where the sample data all clusters near low-index poles. Because of the limited stage-tilt in the TEM, it is not possible to obtain a full range of orientation data. It is clear that the collection of -50°C data was done with the intention of staying well within the stage tilt limits. The room temperature data, on the other hand, is more exploratory and further away from the low index poles. This samples a larger orientation space, but complicates the ability to compare like orientations in different samples because there are more orientations sampled away from low-index poles.

(a)   (b)

-12-

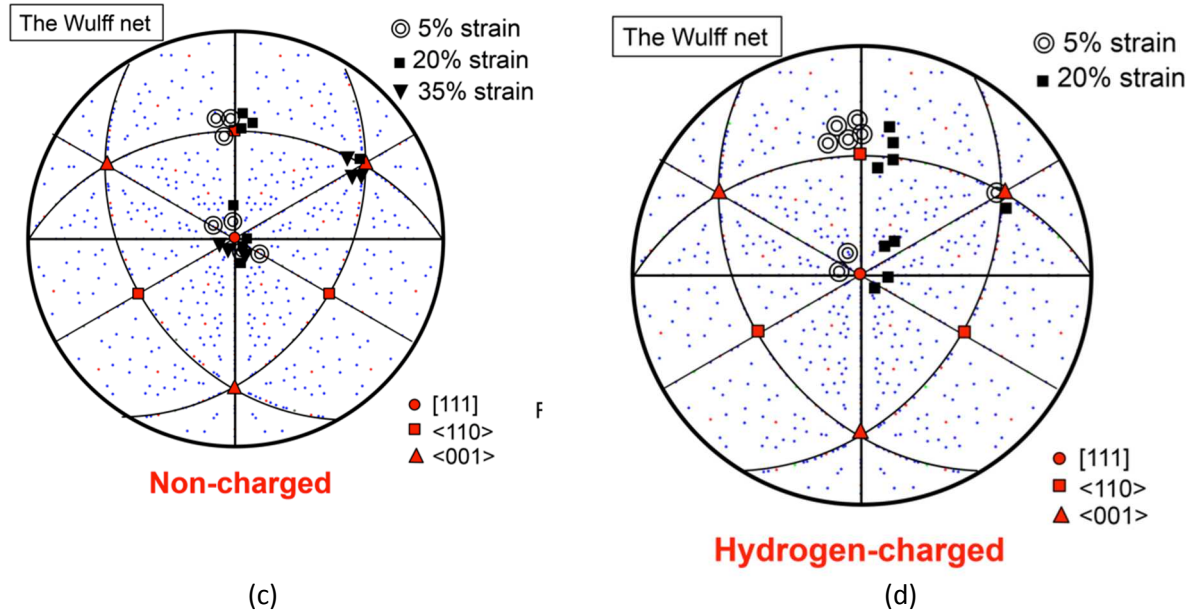(c)   (d)
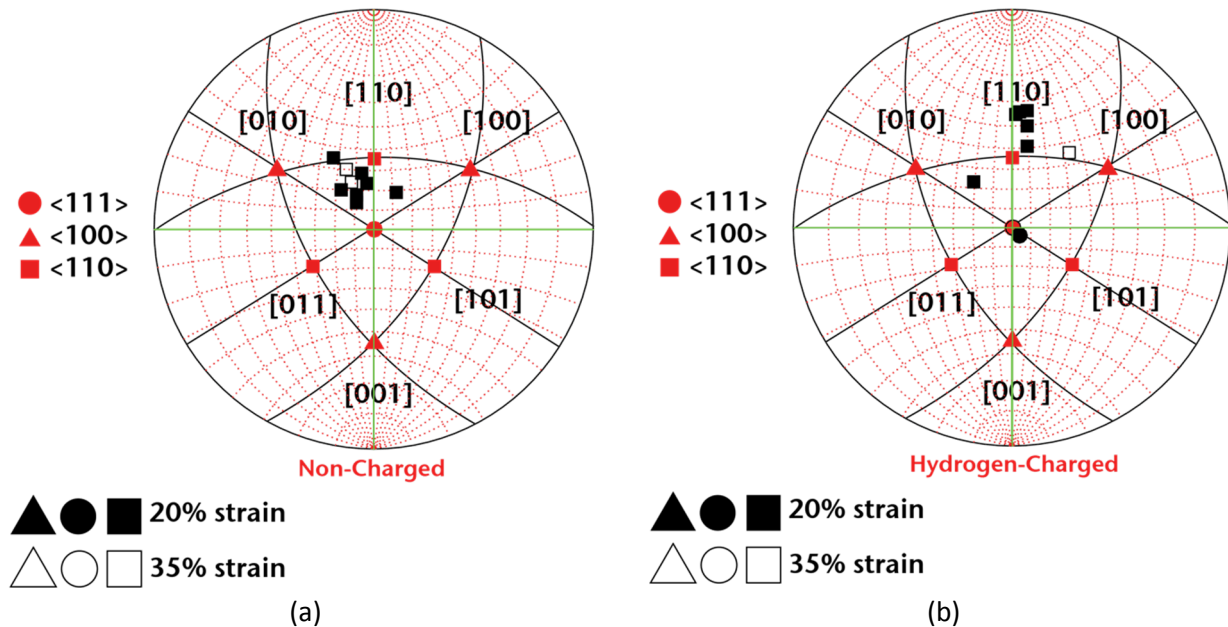
Figure 11: Visualization of grain orientations parallel to the tensile specimen axis using method 1 for specimens at room temperature, (a) and (b), and specimens at -50°C, (c) and (d). The tilt is recorded for every image in the TEM. In each figure, the symbols are plotted close to the pole corresponding to the viewing orientation of the image. For room temperature data, the shape of the symbol refers to the orientation (triangles are <100>-type, squares are <110>-type, and circles are <100>-type) and the symbol is filled for 20% strain, unfilled for 35% strain. For -50°C data, the shape of the symbol refers to strain level, and the orientation is evident by the pole it is clustered around because of limited tilt range of the TEM stage.

The desire for a more straightforward way to compare like orientations for different strain and environmental conditions motivates the development for other methodologies that are more controllable and more systematic. These newer methodologies have not been tried before and required the implementation of new capabilities, which requires some time. However, the progress shown below demonstrates the superiority of the advanced methodologies.

Method 2: The same electropolished TEM foils used for method 1 are used in method 2. An added data acquisition step is performed before the TEM analysis is performed. First, orientation imaging microscopy (OIM) is performed on the TEM specimen to generate an orientation "map". Then, specific grains in the sample are selected for TEM analysis based on their orientation relative to the tensile axis. In this work, there are two options for performing OIM. One is Transmission Kikuchi Diffraction (TKD) and the other is Electron Back-Scattered Diffraction (EBSD). Both techniques are performed in an SEM and are based on the inelastically scattered electrons in the sample forming a divergent source that gets diffracted near the sample surface. These diffraction patterns are recorded on a CCD camera and indexed such that every pixel in an SEM image can be mapped to a specific crystallographic orientation in the sample. For high-quality electropolished specimens, 30 kV electrons transmit through the sample easily and it is possible to use TKD, where the diffraction patterns are formed from electrons transmitted through the sample. When the electropolished TEM foils are of lesser quality and not as thin as desired, EBSD is used, where the diffracted electrons are back-scattered electrons from the sample surface. We will show examples of OIM using both diffraction techniques applied to 21-6-9 with 0 ppm hydrogen in Figure 12.
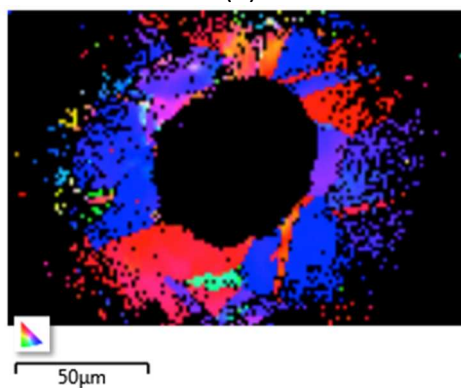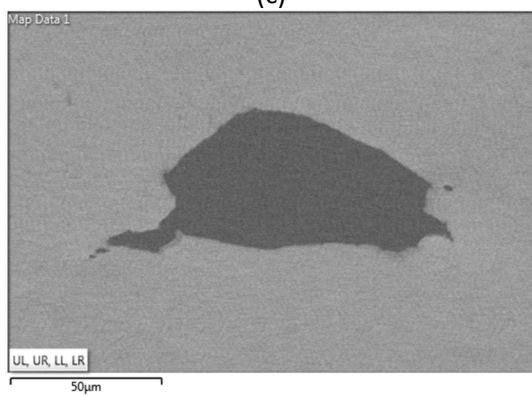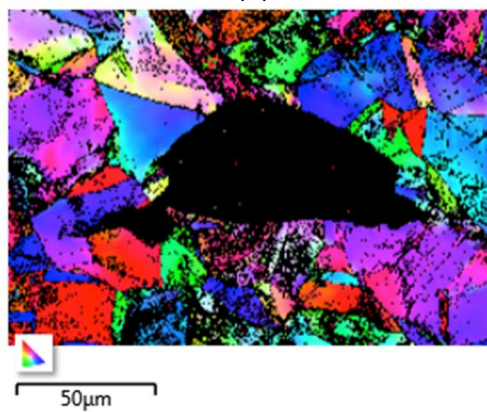
(a)

(b)

(c)

(d)

(e)

(f)

(g)

(h)

Cl Kα1

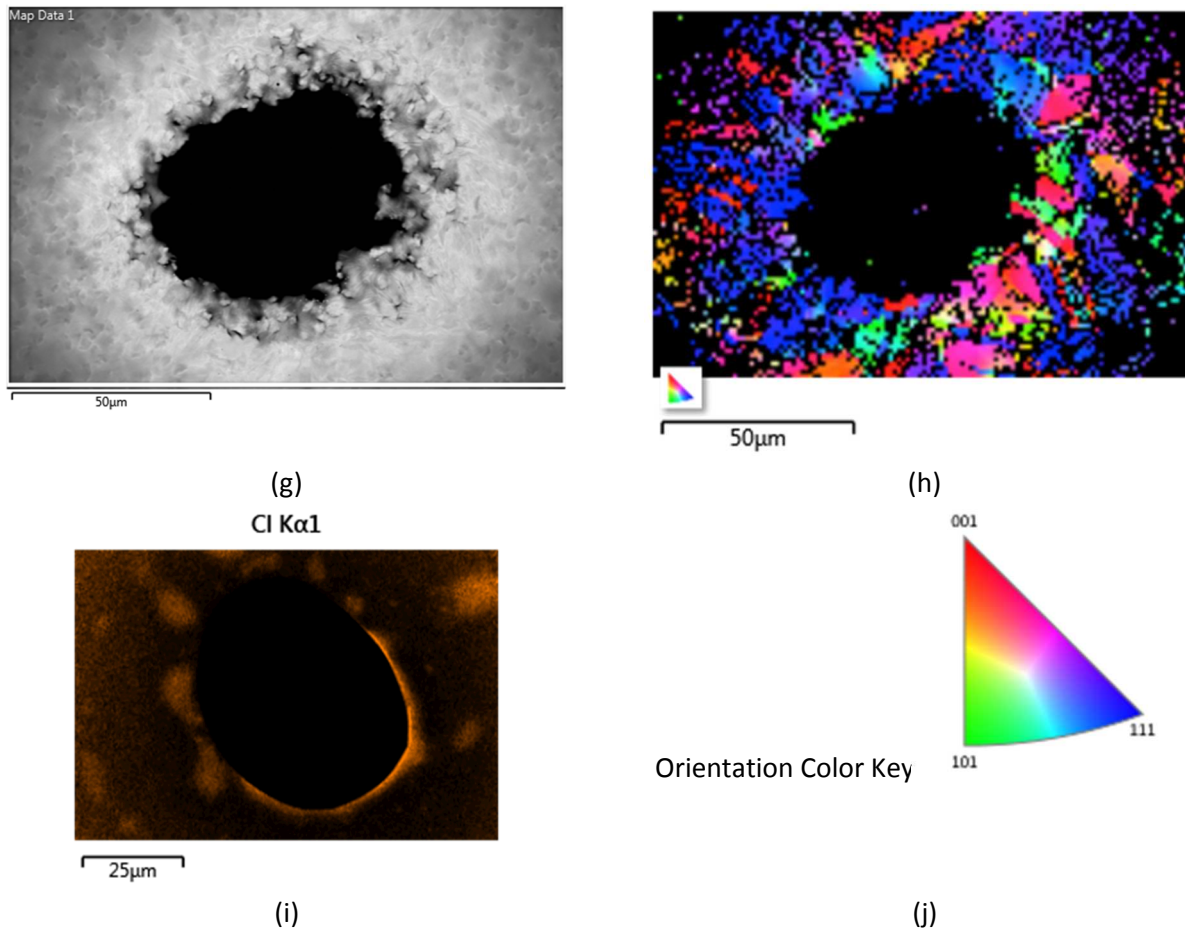
Orientation Color Key

(i)

(j)
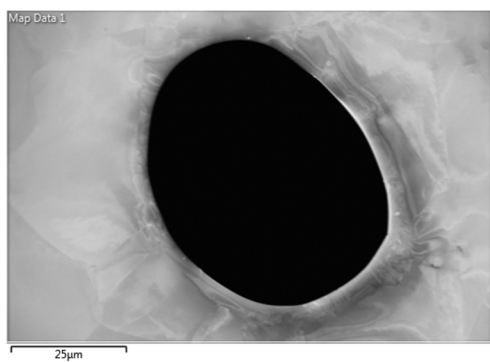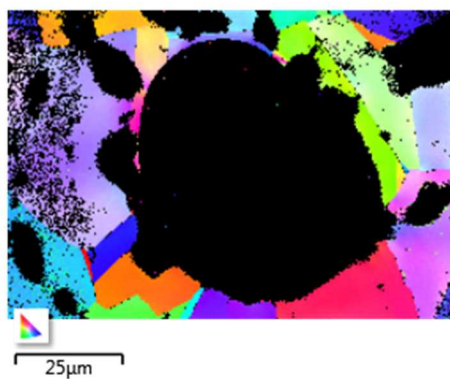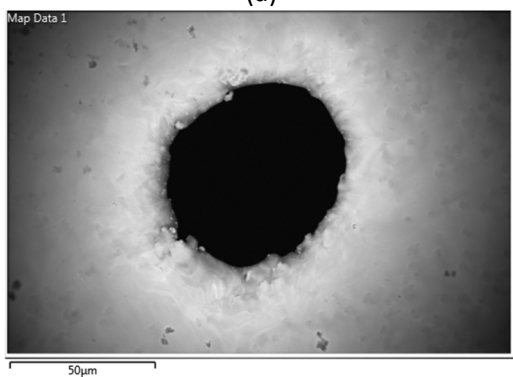
Figure 12: (a) Transmitted electron image of sample strained 5% with 0 ppm hydrogen and (b) corresponding OIM map of sample normal orientation generated using TKD. (c) Transmitted electron image of sample strained 20% with 0 ppm hydrogen and (d) corresponding OIM image of sample normal generated using TKD. (e) Backscattered electron image of sample strained 20% with 0 ppm hydrogen and (f) corresponding OIM image of sample normal generated using EBSD. (g) Transmitted electron image of sample strained 35% with 0 ppm hydrogen and (h) corresponding OIM image of sample normal generated using TKD. In (i), a Cl map of the sample in (a) is shown because Cl from the electrolyte contaminates the surface and causes the dark spots in the OIM map in (b). The orientation color key is shown in (j).

The data in Figure 12 shows that both TKD and EBSD can be used to map the orientation of the grains in electropolished TEM foils. Only (e) and (f) are the result of EBSD, but both techniques are successful at mapping orientation. TKD is more sensitive to sample thickness, thus (d) and (h) quickly lose orientation signal (data becomes black) away from the hole where the sample thickens. EBSD, on the other hand, can map a large region around the hole, but when the sample becomes too thick, it is not electron transparent and TEM is not possible. Therefore, even if EBSD is performed, only the region near the hole can be investigated with TEM. Other artifacts in the OIM result from contaminants on the surface from the electrolytic solution used during polishing. This is seen in Figure 12 (j), where a Cl x-ray map shows Cl-rich regions that correspond with the black regions in (b). This points out the importance of cleaning the sample surfaces well before performing OIM mapping.

As the strain is increased from 5% (Figure 12 (a) – (b)) to 20% (Figure 12 (c) – (f)) to 35% (Figure 12 (g) – (h)), there seems to be an increase in the number of grains with a blue/purple color. The orientation color key shows that the blue/purple orientation is consistent with grains whose <111>direction is aligned with the tensile axis. This suggests that as this material is strained, the grains tend to rotate to align the <111> direction with the tensile axis. It is also possible to see that in the TKD maps, (b), (d), and (h), the quality of the orientation data seems to decrease as evidenced by the increased number of black pixels in (h). Black pixels mean that the diffraction pattern was insufficient quality to be indexed. This could be a direct result of the sample deformation and increase in defects (dislocations and stacking faults) that reduce the quality of the diffraction pattern and increase the difficulty for correctly indexing it. For example, we have shown that streaks form in the electron diffraction pattern observed in the TEM as a result of deformation (for example, Figure 5 (e)). Streaks such as this would cause problems for an automated software algorithm attempting to index the diffraction pattern, and causes the OIM map quality to decrease with increased strain.

Now that we have samples with the orientation of the grains mapped, we can select regions for TEM analysis. This procedure is reflected in Figure 13 for a specimen strained 5% with 0 ppm hydrogen. Some grains were selected for analysis because of their orientation relative to the tensile axis, and because the tilt range of the TEM stage allowed us to achieve a <110> viewing direction. The locations of the images in (b), (c), and (d) are shown in (a). This type of data allows us investigate the effect of grain orientation relative to the tensile axis on the deformation structure. In (b), the grain was oriented such that its <110> direction was roughly parallel to the tensile axis (perpendicular to the sample). In (c) and (d), the purple color of the grain means that the <113> direction was roughly parallel to the tensile axis. A comparison of the observable microstructure in the BF images in (b) and (c) suggests that the dislocation density in the <113> grain is slightly higher. In (c), much more of the viewable area contains dislocations than in (b). A slightly lower magnification in (d) also shows that long straight features resembling stacking faults starting to appear in the image along with some very faint splitting of the spots visible in the diffraction pattern in (d). It is clear from this data that the orientation of the grain relative to the tensile axis definitely affects the deformation structure, as shown here where the dislocation density and formation of stacking faults vary for different orientations.

(a)
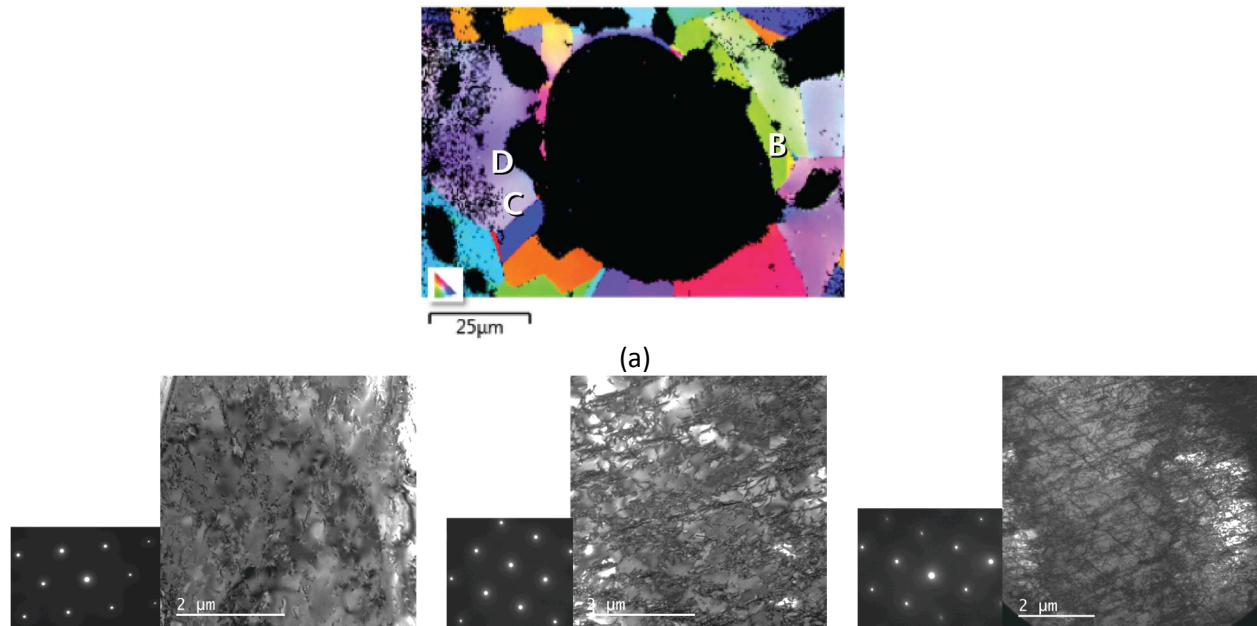
(b)   (c)   (d)

Figure 13: (a) OIM map of sample strained 5% with 0 ppm hydrogen and locations of BF TEM images in (b), (c), and (d) labeled in the image. In (b), the <110> orientation is roughly parallel to the tensile axis, while in (c) and (d), the <113> orientation is approximately parallel to the tensile axis. The image in (d) is a slightly lower magnification than (c), but all BF images are recorded with the viewing direction approximately parallel to the <110> orientation.

A similar exercise was conducted on the sample strained 20% with 0 ppm hydrogen. This is shown in Figure 14. Again, an image is taken from a grain with a <110> orientation closely parallel to the tensile axis and another grain with the <123> orientation closely parallel to the tensile axis. The image in Figure 14 (b) is from a region where <110> is roughly parallel to the tensile axis. In the image, a high density of dislocations is visible, and features that look like stacking faults are also visible, but they are not developed enough to produce streaks in the diffraction pattern. In Figure 14 (c), however, the <123> orientation is roughly parallel to the tensile axis, and definite streaks appear in the <110> diffraction pattern. In addition, slightly wider features resembling stacking/deformation faults are visible in the BF image. Both orientations exhibit high dislocation densities and features that resemble deformation faults. The deformation faults are slightly more developed when the <123> orientation is parallel to the tensile axis as evidenced by the streaks in the diffraction pattern, which do not appear when the <110> orientation is parallel to the tensile axis.

The ability to perform OIM mapping prior to performing TEM is powerful in that it allows us to select regions to focus our TEM analysis time on. However, we are still subject to the randomness of the grain orientations in the electropolished TEM foils. Additional control is provided in method 3.
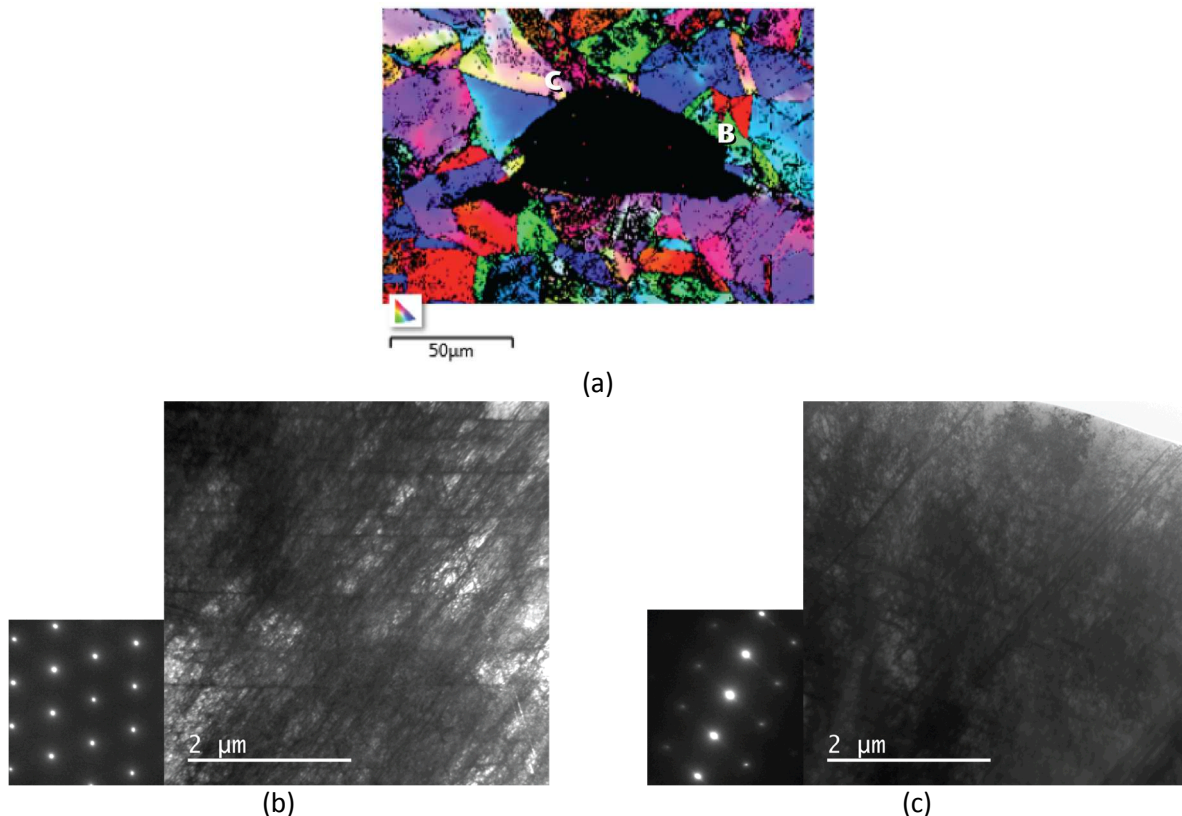

(a)

(b)   (c)

Figure 14: OIM map of sample strained 20% with 0 ppm hydrogen and locations marked for images in (b) and (c). The corresponding BF images and <110> type diffraction patterns are shown in (b) and (c). The

viewing direction is parallel to the <110> direction. The defects in (c) running from the lower left to the upper right of the image are slightly more developed than those in (b), which results in streaks in the diffraction pattern.

Method 3: We simply did not have time to develop method 3 all the way from start to finish this year. This was out of the project scope for this year. We have shown that we can perform OIM mapping on a region of the tensile bar using EBSD as in Figure 15. We have not yet performed FIB liftout on a selected region of this sample. However, it is important to point out that the liftout can be performed with much more control of the sample orientation. This means that the liftout can be done in a way such that the viewing direction to the liftout can be parallel to a <110> direction regardless of the grain orientation relative to the tensile axis. This is because in method 2, the tilt range of the TEM stage limits our viewing direction for any particular grain. The <110> orientation is the preferred viewing direction because 4 {111} planes are edge on in this orientation and these planes are parallel to the stacking faults. A <110> viewing direction cannot be obtained in every grain in method 2 because of limited stage tilt. In method 3, however, careful geometric considerations can be accounted for and it is possible to obtain a <110> viewing direction for a grain with any orientation relative to the tensile axis. For this reason, method 3 provides the highest level of control and will be developed further in the future.
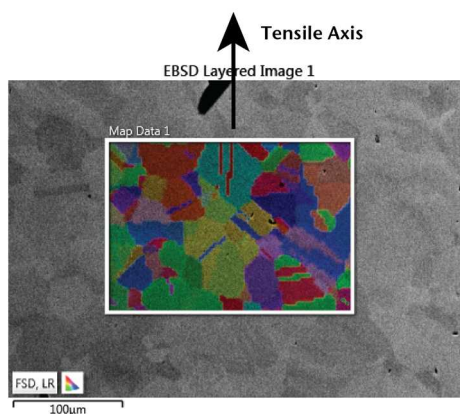

Figure 15: EBSD map of section of tensile bar strained 5% with 0 ppm hydrogen. The next step is to perform FIB liftout on selected grain orientations.

Conclusions and Future Work

[Provide closing statement including recommendations for application and future work]

This year, we have developed a hypothesis for the effects of environment on deformation mechanisms in 21-6-9 austenitic stainless steels. We propose that the deformation is accompanied by the formation of dislocations, which eventually separate into stacking faults. The stacking faults then widen as additional dislocations add one atomic plane at a time to the fault, eventually forming a deformation twin. The presence of hydrogen reduces the ability for the dislocations to cross slip and glide, resulting in thinner twins that may contribute to microcrack formation. In the future, we will continue to develop our new capabilities and methodologies to test our hypothesis and refine it to account for effects of grain orientation on twin characteristics such as thickness. Ultimately, understanding the deformation mechanism is a critical step in the development of predictive hydrogen-assisted cracking models that can be used to evaluate the long-term aging performance of stainless steels in hydrogen isotope environments relevant to GTS. The continued work to develop methods and capabilities to characterize

the deformation phenomena active during straining of these materials is necessary for understanding aging and long-term performance of structural metals in hydrogen environments.

Summary of Findings and Capabilities Related to Aging

- We developed a hypothesis that describes the deformation mechanism in 21-6-9 stainless steel. Understanding the effects of hydrogen and temperature on this mechanism is crucial to developing models that predict the long-term aging performance of these materials in GTS service environments.
- We investigated samples strained at -50°C and found that low temperature does not appear to alter the deformation characteristics in 21-6-9 stainless steel with either 0 ppm or 220 ppm hydrogen. This observation suggests that any effect of low temperature on hydrogen-assisted cracking is not related to changes in the material deformation.
- We developed new capabilities at the CA site that will enable more systematic and controllable investigations of the effect of strain, environment, and crystallographic orientation on the deformation structures. Specifically, these include orientation imaging microscopy (OIM), and focused ion beam (FIB) machining.
- We used OIM to compare deformation structures in grains with different orientations relative to the tensile axis. We found that the development of twinned or deformation faults can be slightly accelerated for some specific orientations. A more systematic study of orientation is needed in future work.

References

[1] B.P. Somerday, *et al.*, *Metallurgical and Materials Transactions a-Physical Metallurgy and Materials Science* **40A** (2009)
[2] K.A. Nibur, *et al.*, *Acta Materialia* **57** (2009)
[3] B. Clausen, *et al.*, *Materials Science and Engineering: A* **259** (1999)
[4] T.S. Byun, *Acta Materialia* **51** (2003)
[5] K.A. Nibur, *et al.*, *Acta Materialia* **54** (2006)
[6] P. Mullner and C. Solenthaler, *Materials Science and Engineering a-Structural Materials Properties Microstructure and Processing* **230** (1997)
[7] P. Mullner, *et al.*, *Acta Metallurgica Et Materialia* **42** (1994)

Administrative Addendum

- **Related Publications and Presentations:**

Junko Matsuda1, Josh Sugar2, Mark Homer2, Douglas Medlin2 and Brian Somerday1,2, Effect of Hydrogen on Deformation Behavior of 21Cr-6Ni-9Mn Austenitic Stainless Steels, Presented at FEMS EuroMAT 2015, Sep. 20-24, Warsaw, Poland.

- **Milestone Status:**

- Complete characterization of deformation microstructures in stainless steel as function of strain and hydrogen concentration (09/30/2015). This milestone was completed in FY15 based on conventional methods for characterizing deformation microstructures.